COMPUTATIONAL MODELING OF HEMODYNAMICS AND BLOOD WASHOUT IN THE PATIENT-SPECIFIC LEFT ATRIAL APPENDAGES

by

Chuanxin Ni

A thesis submitted to The Johns Hopkins University

in conformity with the requirements for the degree of

Master of Science in Engineering

Baltimore, Maryland

May, 2019

Abstract

The left atrial appendage (LAA) is a small chamber-like organ connected to the left atrium (LA) of the heart. Studies have shown that this structure is implicated in thrombus formation and thromboembolic events for patients with the atrial fibrillation (AF). However, due to the highly complex and variable shapes, the blood flow pattern and mechanism of thrombogenesis inside the LAA are poorly understood. This study aims to analyze the hemodynamics in the LAA and establish an approach to predict the potential of thrombus formation in the LAA. Four patient-specific LA/LAA anatomical models and four scaled LAA models are derived from computed tomography (CT) scans and the corresponding blood velocity profiles at the mitral valve orifices are obtained from ultrasound Doppler measurement for boundary conditions. Several direct numerical simulations are carried out using a sharp-interface immersed boundary method (IBM). From the flow field analysis, it is found that the velocity and vorticity magnitude in the LAA are relatively low, which indicates a more stagnant blood flow in the LAA. The LAA hemodynamic metrics are then defined based on the clinically measurable parameters of the patient-specific LAA morphology and the averaged and highest flow intensity

in the LAA. The transport of a passive scalar in the LAA is also solved to investigate the blood washout rate in the LAA. Based on the evolution of the scalar, the blood washout rate metrics are defined by the decay rate or final values of the volume-averaged scalar concentration in the LAA. Finally, correlations are derived between the two groups of metrics and the best correlation is found to be between the decay rate of the volume-averaged scalar concentration in the LAA and the metric associated with the hemodynamics at the neck region of the LAA. Using this correlation, it may be possible to predict the blood washout rate and the potential of thrombus formation in the LAA for more effective individualized therapies.

Keywords*: Left Atrial Appendages, Blood Washout Rate, Hemodynamic Metrics, Immersed Boundary Method, Computational Fluid Dynamics*

Primary Reader and Advisor: Jung-Hee Seo

Secondary Reader: Rajat Mittal

Acknowledgments

I would like to first express my deep gratitude to my primary academic advisor Professor Jung-Hee Seo of Department of Mechanical Engineering. He was always generous to give his time and hold a weekly meeting with me. This really helped me solve the problems I came across and profoundly paved the way to my thesis research. My grateful thanks are also extended to my secondary academic advisor Professor Rajat Mittal of Department of Mechanical Engineering. He was always willing to share his experience in this research arena and his insights into the research topic could always steer me into the right direction. I also took several numerical methods courses taught by him, from which I obtained the crucial knowledge of the numerical tools for this research. I would also like to acknowledge Dr. Thura T. Harfi of Department of Medicine at Ohio State University for his help in obtaining the CT scans for the thesis. My thanks also go to my colleagues in the FPCL. They helped me a lot in setting up the CFD simulations. Supports from Department of Mechanical Engineering are also greatly appreciated. Finally, I wish to thank my parents for the encouragement and comfort they gave to me when my research went into some troubles. Without the help above, I will not be able achieve this accomplishment.

Table of Contents

List of Tables

List of Figures

Chapter 1

Introduction

The atrial fibrillation (AF), the most common cardiac arrhythmia, usually causes the dysfunction of the left atrium (LA), making it lose the ability to contract properly and rhythmically[1]. Patients with AF often experience rapid and irregular heartbeats, which change the hemodynamics in the LA and cause blood stagnation in the left atrial appendage (LAA)[2, 3]. This abnormal LA behavior has been found to be the leading cause of thromboembolic events, such as strokes and vascular dementia[4]. It is also found that among patients with AF, over 90% of LA thrombi are formed inside the LAA[5]. Therefore, studying the function of the LAA and finding clinical solutions for the above problem have been an increasingly crucial issue in the arena of LA disease research.

The LAA, which is a protruding chamber starting from the muscle wall of the LA, has a highly variable morphology from patient to patient, and this makes it difficult to characterize the shapes[5]. The huge variation of patient-specific geometry of the LAA, coupled with the complex hemodynamics inside, make it even more difficult to determine the role of this chamber in

the function of the LA[6], so it is hard to apply generally effective therapies to patients. Currently, there are two available therapeutic options to reduce the risk of thrombogenesis in the LAA: (i) oral anticoagulation; and (ii) surgical exclusion or occlusion of the LAA[5]. Unfortunately, though both options may be effective for certain groups of patients, they both have their own drawbacks. On the one hand, oral anticoagulation may increase the hemorrhagic risk for some patients[7, 8]. On the other hand, surgical exclusion or occlusion of the LAA may cause unintended consequences, as the function of the LAA still remains unknown[6] and the surgeries are highly complicated[5]. Thus, a preferred clinical option for this problem is to apply individualized treatments to prevent or reduce the potential of thrombus formation in the LAA.

Individualized treatments for patients will bring forth the demand for a method to predict the current risk of thrombogenesis in the LAA. However, an effective method for this has not been established yet. One possible method is to classify the morphology of the LAA. According to Ref. [3], the shape of the LAA is typically classified into four types: chicken wing, windsock, cactus and cauliflower. It is known that non-chicken-wing LAA morphology has a higher possibility than a chicken-wing type to experience blood stagnation and thrombus formation[3, 9]. Nevertheless, distinguishing one LAA geometry from another is a subjective process and even among cardiovascular morphology specialists, an agreement of classification is hard to reach[6]. Moreover, in addition to the shape of the LAA, different patient-specific blood flow conditions can also play an important role on the thrombus formation in the LAA. Therefore, a method based solely on LAA morphology may not be

an effective way to predict the risk of thrombogenesis in the LAA.

Some other researchers explored the relation between the hemodynamics (especially the blood flow velocity) and thrombogenesis in the LAA. It is found that low velocity in the LAA are related to a higher risk of thromboembolic events[2, 10]. However, blood flow velocity is usually measured from transesophageal echocardiographic (TEE) images and velocity information is only available on a plane (e.g. LAA ostium) or at a certain spatial point (e.g. LAA center)[6]. The comprehensive blood flow field in the entire LA for one cardiac cycle cannot be obtained from the above measurement. This kind of limited blood flow information may only provide a relatively simple index and is unable to characterize the complicated hemodynamics in the LAA. Some other measurement methods (e.g. 4D-flow magnetic resonance imaging (MRI) technique) are expected to give more complete blood flow information, but they are still in development.

Computational modeling approaches are good alternatives to obtain comprehensive blood flow field information in the LA/LAA. These methods have been successfully applied to other cardiovascular problems such as coronary artery diseases[11], the thrombogenesis in the left ventricles (LV)[12], and the surgical planning for Fontan diseases[13]. There are several papers in the literature using CFD to investigate the LAA thrombogenesis problem, but most of them are based on synthetic LAA configurations or only one or two patient-specific LAA anatomical models[5, 6, 14, 15, 16].

Although there are studies ongoing on this topic, few of the previous studies combined patient-specific LAA morphology with the corresponding

blood flow field in simulations and analyses. Few studies if any have proposed metrics to quantify the blood washout rate in the LAA, which is a direct evaluation of the blood stagnation in the LAA. Correlations are also lacking between the above metrics and patient-specific hemodynamics and morphology of the LAA, which can be used to predict the blood washout rate as well as the risk of thrombogenesis in the LAA.

In the present study, four patient-specific models and the corresponding blood flow conditions are employed to investigate the hemodynamics and blood washout in the LAA by using DNS and IBM. In addition, four scaled LAA anatomical models are also considered to study the effects of LAA size. The simulated flow field are first examined, and the velocity and vorticity magnitude are shown in plots to investigate the hemodynamics in the LAA. From the observations, two clinically measurable LAA hemodynamic metrics are then proposed based on the LAA morphology and the averaged and highest velocity strength inside the LAA. To analyze the blood washout in the LAA, a passive scalar is initially âĂIJfilledâĂİ in the LAA and the evolution of this scalar is simulated by an advection-diffusion equation. Based on the passive scalar transport, two metrics are then defined to quantify the blood washout rate in the LAA. Correlations between the hemodynamic metrics and the washout rate metrics are subsequently calculated. Finally, based on the correlations, it is shown that one may use the LAA hemodynamic metrics to estimate the degree of patientsâĂŹ blood washout rate in the LAA so as to predict the potential of thrombogenesis in the LAA.

Chapter 2

Materials and Methods

2.1 LA/LAA Anatomical Models

The patient-specific geometry of the left heart is obtained from the anonymous CT scans in collaboration with the Johns Hopkins Hospital. The patient cases we used were initially scanned for left ventricle thrombogenesis problems without any known left atrial pathologies. Thus, the present study is focused on the patient-specific blood washout rate in the LAA and its correlations with the hemodynamics in the LAA rather than direct identification of LA/LAA pathologies. Some important information of each case is listed in Table 2.1.

Table 2.1: Important information of each patient case

	Patient-1	Patient-2	Patient-3	Patient-4
Stroke Volume (SV) (cm^3)	81.29	124.28	155.80	100.96
LA Volume (V_{LA}) (cm^3)	46.19	103.84	104.32	78.14
LAA Volume (V_{LAA}) (cm^3)	1.71	4.30	7.42	3.93
LAA Neck Area (S_{neck}) (cm^2)	0.82	2.17	1.84	1.35
Heart Rate (HR) (bpm)	52.00	55.00	60.00	70.00
E/A Ratio	1.76	1.26	0.74	0.65

The CT scan data are segmented in the commercial software Materialise

Mimics for the LA/LAA by using a masking function. The masking function for each case is generated by a dynamic region growing method with a suitable threshold difference. This raw masking function is then smoothed and wrapped to filter out unnecessary and non-physical minor details. The 3-D reconstruction of anatomical models based on the masking functions are then created for each case as shown in Figure 2.1.

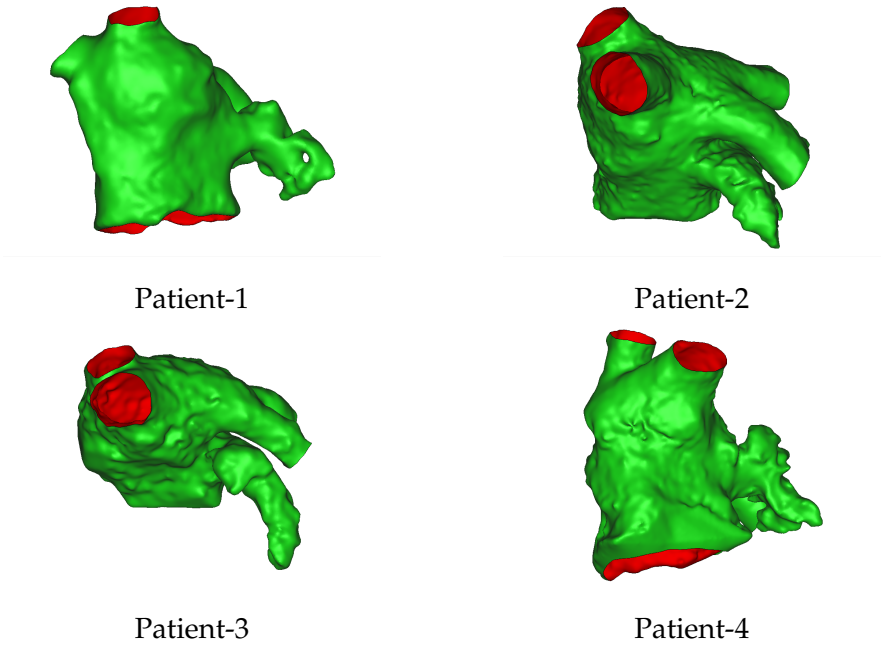

Figure 2.1: LA/LAA anatomical models

These cases are chosen specifically to include typical LAA shape types, which are the Chicken wing models (Patient-1, Patient-4), the Cactus model (Patient-2) and the Windsock model (Patient-3). For each case above, the pulmonary veins (PV) are cut off perpendicularly to form openings around their first bifurcations and the mitral valve orifice (MVO) is created manually based on the anatomical structure. To simplify the application of boundary

conditions, the outline of all the openings is extruded naturally to form tubes with a suitable length. Each model is then fit into a Cartesian domain for the IBM simulations. The unstructured surface meshes for the 3-D anatomical models above are generated by another commercial software Materialise 3-matic with triangular elements for the internal solid boundaries. The surface mesh for each case is constructed with over 40,000 elements to accurately resolve critical anatomical structures.

2.2 Numerical Methods

The flow simulations are performed with an in-house immersed boundary based flow solver[17]. The blood flow is simulated by solving the incompressible Navier-Stokes (INS) equations (Eq. 2.1) with a direct numerical simulation (DNS) method.

$$\begin{aligned} \nabla \cdot \vec{u} &= 0 \\ \frac{\partial \vec{u}}{\partial t} + (\vec{u} \cdot \nabla)\vec{u} &= -\frac{1}{\rho}\nabla p + \nu \nabla^2 \vec{u} \end{aligned} \tag{2.1}$$

In Eq. 2.1, $\vec{u}$, t, ρ, p, ν denote for the blood flow velocity, time, blood density, flow pressure and blood kinematic viscosity, respectively. The INS equations are solved by a sharp-interface immersed boundary method in order to handle the complex LA/LAA geometry. A projection method[18] is used for the velocity-pressure coupling and second order numerical schemes are applied for temporal and spatial discretization. For the Pressure Poison Equation, the bi-conjugate gradient (BiCG) method is implemented to speed up the process of solving the linear system[19].

2.3 Boundary Conditions

The surface meshes of the 3-D anatomical models shown above are taken as internal solid boundaries. Although, for real cases, LA/LAA are deformable during one cardiac cycle, we assume that the LA/LAA walls are stationary in the present study. The impact and limitations about this treatment will be discussed in the Limitation section. A no-slip condition is imposed on those internal boundaries. At all inlets of the PV tubes, a zero-gradient boundary condition is imposed for the axial velocity. While, at the outlet, patient-specific velocity profiles are assigned to the axial velocity of the MV tube as a prescribed Dirichlet condition. In order to obtain the velocity profiles, ultrasound Doppler measurement of the time history of the blood flow velocity through the MVO as well as the E-wave/A-wave (E/A) ratio for each case (see Figure 2.2) are used. The MVO velocity profiles usually have two peaks in each cardiac cycle; the first peak is the E-wave and the second one is the A-wave. They correspond to the expansion of the LV and the contraction of the LA respectively. Based on the E/A ratios and the left ventricle stroke volume calculated from the CT scans, exponentially altering sinusoidal functions are then used to reconstruct the patient-specific velocity profiles at the MVO (see Figure 2.2). This method is based on the Simple Harmonic Oscillator (SHO) Model which has been verified with the patient data in Ref. [20].

For the radial and the tangential velocity components at the outlet of the MV tube, a zero-gradient, slip condition is imposed.

As for the pressure boundary conditions at the inlets and the outlet, the zero-gradient condition is used again.

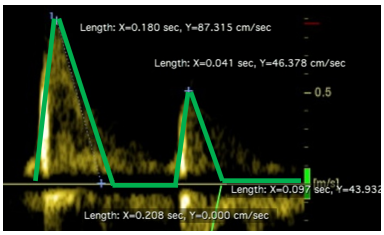

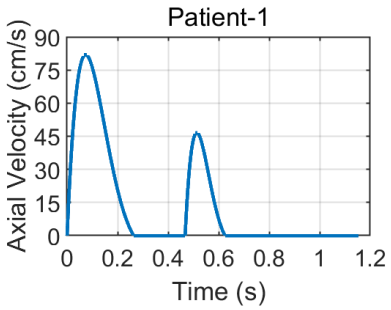

Patient-1, $E/A = 1.76$

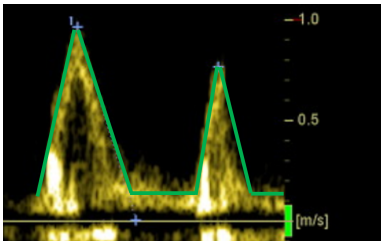

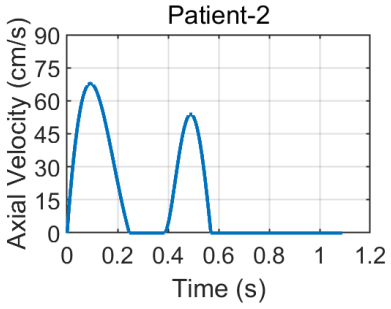

Patient-2, $E/A = 1.26$

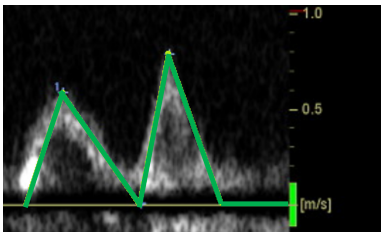

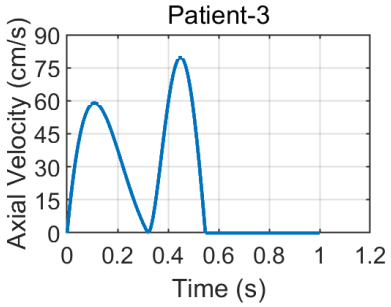

Patient-3, $E/A = 0.74$

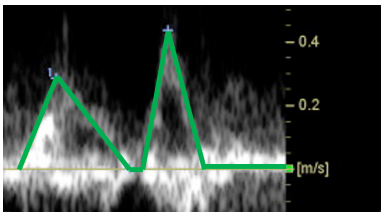

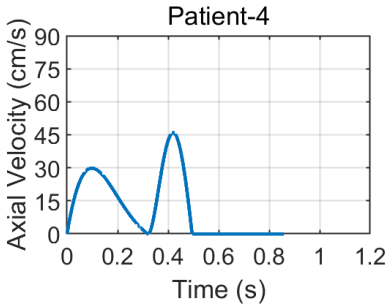

Patient-4, $E/A = 0.65$

Figure 2.2: Ultrasound Doppler measurement and reconstructed velocity profiles

2.4 Characteristic Parameters

To parameterize the simulations, the maximum diameter of the MVO for each case is chosen as the characteristic length scale D, and the time averaged axial velocity at the outlet of the MV tube during each cardiac cycle is selected as the characteristic velocity scale V. The flow Reynolds number (Re) is then defined as $Re = VD/\nu$, where ν is selected to be $3.8 \times 10^{-6}\ m^2/s$, a typical value for blood kinematic viscosity. For the cases in the present study, Reynolds numbers vary between 1235 to 2013. The time step size in real dimension, $dt = 1 \times 10^{-4}\ s$, is used for the simulations and the non-dimensional time step size then vary from 2.8×10^{-4} to 6.2×10^{-4}.

2.5 Passive Scalar in the LAA

A passive scalar is initially filled into the LAA of each case (see Figure 2.3). Acting like a fluid dye, the passive scalar is able to represent the convection and diffusion of blood and provide quantitative information about the blood washout rate in the LAA. In Figure 2.3, C denotes for the scalar concentration.

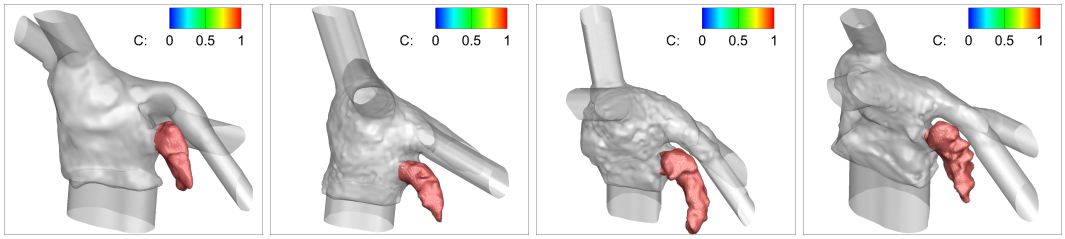

Patient-1 Patient-2 Patient-3 Patient-4

Figure 2.3: Initial condition for passive scalar

The evolution of the passive scalar is calculated by solving an advection-diffusion equation (Eq. 2.2) which represents the transport of the scalar in the Eulerian frame of reference.

$$\frac{\partial C}{\partial t} + u_j \frac{\partial C}{\partial x_j} = \frac{1}{Re \cdot Sc} \frac{\partial}{\partial x_j} \left(\frac{\partial C}{\partial x_j} \right) \tag{2.2}$$

In the Eq. 2.2, x, Re, Sc denote for the general spatial coordinates, Reynolds number and Schmidt number, respectively. The Schmidt number for all the cases in the present study is one. Though the Schmidt number for real chemicals in humanâĂŹs blood can have a different value, the main focus of the present study is to simulate the transport of a general scalar and develop an approach to correlate the LAA blood washout rate metrics with the LAA hemodynamic metrics. Once the approach is validated, more simulations with different Schmidt number can then be carried out for any specific condition. After the simulations are completed, the patient-specific blood washout rate in the LAA is quantified based on the decay rate of volume-averaged scalar concentration (C_{va}) inside the LAA or the final values of the C_{va} in the LAA.

2.6 Simulation Procedures

To perform the blood flow/passive scalar transport simulations, all the cases are started with two patient-specific cardiac cycles to achieve the fully developed blood flow field. Then, all the simulations are continued with additional four patient-specific cardiac cycles including the scalar transport. After six cardiac cycles in total for each case, all the data are collected for the analysis in the Results and Discussions section.

Chapter 3

Results and Discussions

3.1 Velocity Magnitude

One of the main objectives of the present study is to find the correlations between the LAA hemodynamic metrics and the blood washout rate metrics in the LAA. Therefore, to define the LAA hemodynamic metrics, the patient-specific blood flow field should be examined first and some variables relating to the hemodynamics in the LAA should be proposed. In Figure 3.1, four frames of contour plots of the velocity magnitude in one cardiac cycle are presented. The contour plots are shown on the plane across the LA and the LAA for each case at time instances of E-wave peak, E-wave end, A-wave peak and A-wave end.

During the time period of the E-wave peak, the MV is open and blood flows out of the LA through the MVO. For the present simulated cases, the blood flows are driven out from the LA by the prescribed velocity boundary conditions at the MVO. During the E-wave period, the velocity magnitude in the LA can reach a relatively large value but the velocity magnitude in the

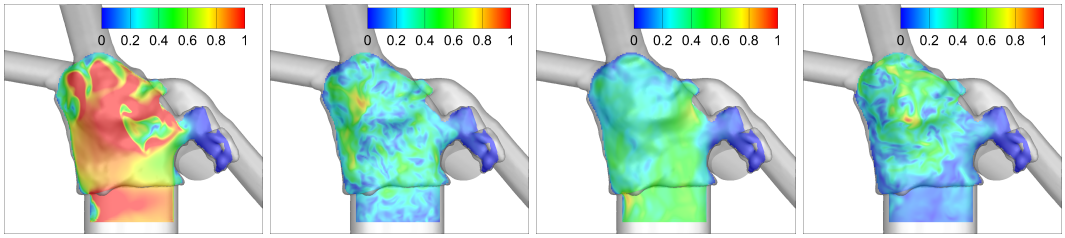

E-wave Peak E-wave End A-wave Peak A-wave End

Patient-1, $E/A = 1.76$

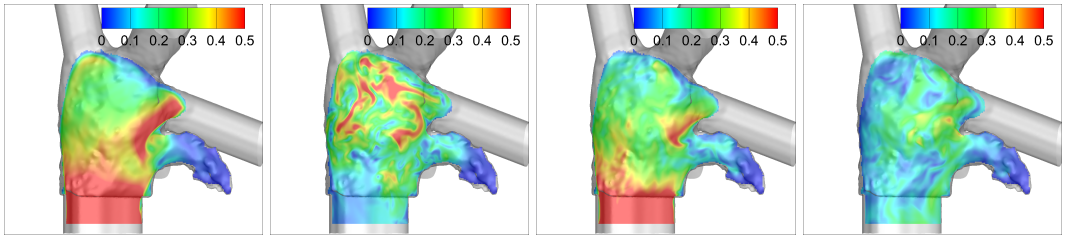

E-wave Peak E-wave End A-wave Peak A-wave End

Patient-2, $E/A = 1.26$

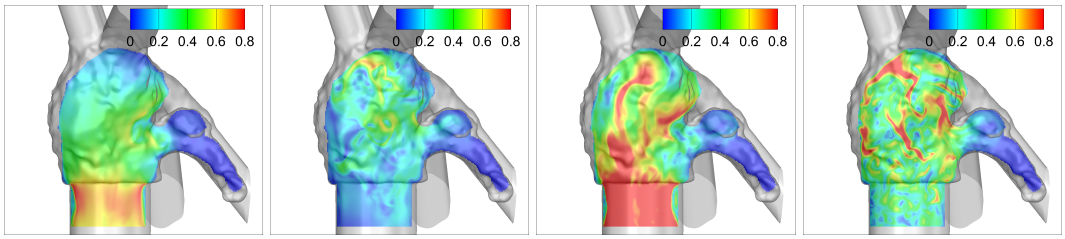

E-wave Peak E-wave End A-wave Peak A-wave End

Patient-3, $E/A = 0.74$

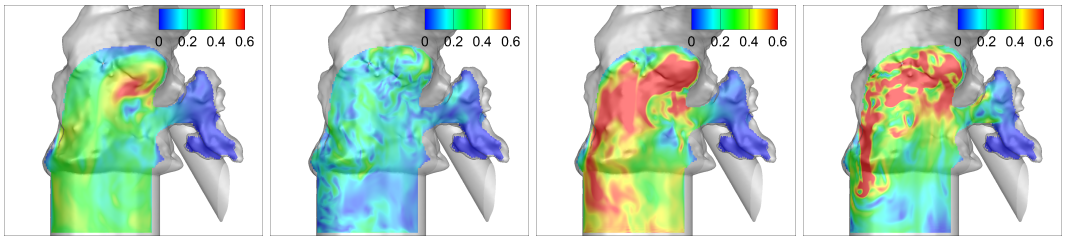

E-wave Peak E-wave End A-wave Peak A-wave End

Patient-4, $E/A = 0.65$

Figure 3.1: Contour plots of velocity magnitude (m/s)

LAA remains small. The high velocity in the LA cannot propagate deep into the LAA. As the MV closes around the E-wave end, the blood flow intensity inside the LA is dissipated by viscous effects, so the velocity magnitude in the LA decreases as well. At the same time, the velocity magnitude in the LAA still remains a small value. Similarly, during the A-wave period, the velocity magnitude in the LA will increases and decreases again by similar effects, but the velocity magnitude in the LAA will remain at a relatively small value all along the A-wave period. Comparing the four cases in Figure 3.1, one obvious difference among the cases is that the peak velocity magnitude of each case happens at different time instances. Since the E/A ratios of the Patient-1 and Patient-2 cases are larger than one, the velocity magnitude in the LA of them has a higher value around the E-wave peak than around the A-wave peak. On the contrary, as the E/A ratios of the Patient-3 and Patient-4 cases are smaller than one, the velocity magnitude in the LA of them around the E-wave peak now is smaller than that around the A-wave peak.

Generally, it is observed that the velocity magnitude inside the LAA is relatively small compared to that in the LA. It is also clear that the velocity magnitude at the neck of the LAA can reach a relatively large value. As you go deeper into the LAA, the velocity magnitude will keep decreasing and reaches its smallest values at the tip of the LAA.

3.2 Vortical Structures

In Figure 3.2, four frames of the iso-surface plots of the second invariant of velocity gradient (Q) for each case are presented to visualize the vortical

structure in the LA/LAA at the same four time instances as in Figure 3.1. The plots are colored by vorticity magnitude with patient-specific ranges so we can see the distribution and compare the value of it at different locations.

Comparing with the contour plots of the velocity magnitude in Figure 3.1, similar developing trends of the vorticity as well as the vortical structures in the LA/LAA can be observed in Figure 3.2. At the beginning of the E-wave period, the vorticity starts to increase and the vortical structures begin to be generated in the LA as the flows are driven out from the LA by the prescribed velocity boundary conditions at the MVO. Relatively large vorticity magnitude can be observed in the LA, but it remains a small value inside the LAA. After the E-wave peak, the vorticity starts to be dissipated by viscous effects and the vorticity magnitude begins to decrease. At the end of the E-wave period, the MV is closed and the vorticity magnitude will keep decreasing to a small value until the start of the A-wave period. Similar developing patterns of the vortical structures as well as the vorticity magnitude will be observed during the A-wave period but with different peak vortical intensity. For Patient-1 and Patient-2, since their E/A ratios are larger than one, the peak vortical intensity around the A-wave peak is lower than that around the E-wave peak. On the contrary, for Patient-3 and Patient-4, as their E/A ratios are smaller than one, they will have a higher peak vortical intensity around the A-wave peak than around the E-wave peak.

Some general conclusions can be drawn from the plots in Figure 3.2. Though strong vorticity is observed in the LA, the vorticity in the LAA is relatively weak and the strong vorticity in the LA does not propagate far into the

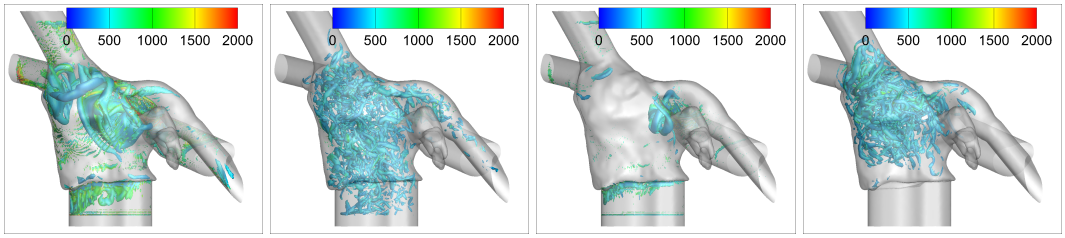

E-wave Peak E-wave End A-wave Peak A-wave End

Patient-1, $E/A = 1.76$

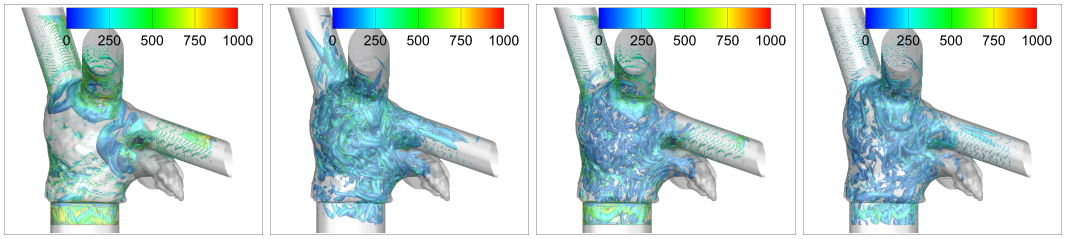

E-wave Peak E-wave End A-wave Peak A-wave End

Patient-2, $E/A = 1.26$

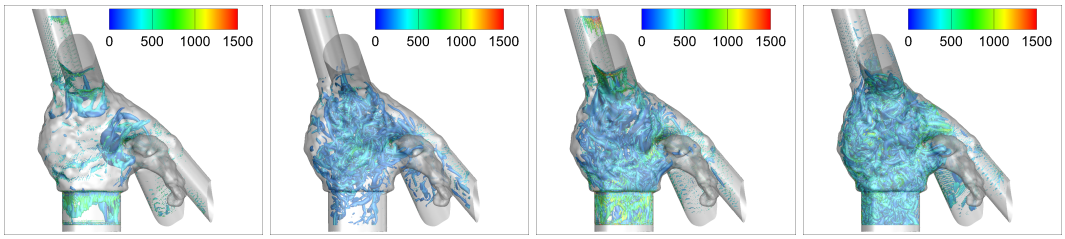

E-wave Peak E-wave End A-wave Peak A-wave End

Patient-3, $E/A = 0.74$

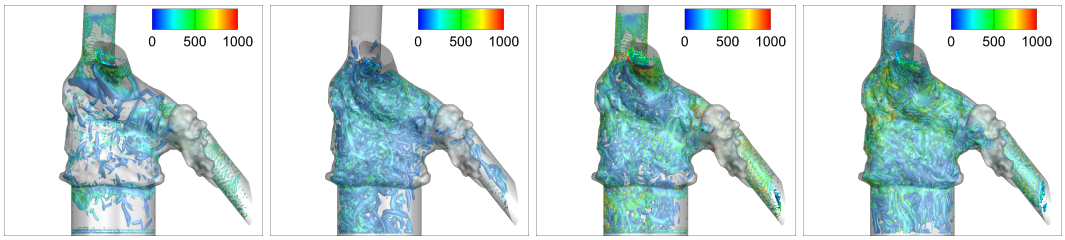

E-wave Peak E-wave End A-wave Peak A-wave End

Patient-4, $E/A = 0.65$

Figure 3.2: Iso-surface plots of Q colored by vorticity magnitude $(1/s)$

LAA. Similar to the velocity filed in Figure 3.1, the vorticity magnitude near the neck of LAA can reach a relatively larger value, but as you go deeper into the LAA, the vorticity magnitude will keep decreasing to its smallest values at the tip. Moreover, if we combine the results from the previous section, it is also clear that the blood flows are more stagnant inside the LAA than outside, which may represent a higher potential of thrombus formation. Similar results and conclusions can also be found in the literature[14].

From the analyses of the velocity magnitude and the vortical structures above, one can find that the highest flow intensity is at the neck region of the LAA. The deeper you go into the LAA, the lower the flow intensity will be. According to the flow intensity distribution in the LAA, one intuitive way to define the LAA hemodynamic metrics is to define them based on the averaged or the highest flow intensity in the LAA. Thus, some variables relating to the highest flow intensity at the neck region or the averaged flow intensity over the entire LAA can be proposed as the LAA hemodynamic metrics. To get these candidate variables, a more quantitative analyses of the flow intensity at the neck region and over the entire LAA are shown in the next section.

3.3 Averaged Velocity Curves

In this section, the analyses of the flow intensity at the neck region and inside the LAA is presented. To quantify the flow intensity at one location, a good method is to use some velocity strength variables. Thus, two averaged velocity variables, v_{ave} and v_{neck}, are proposed to evaluate the velocity strength at the two locations, respectively. The exact definitions of v_{ave} and v_{neck} are presented

in Eq. 3.1 and Eq. 3.2.

$$v_{ave} = \frac{\int_{LAA} |\vec{u}|\, dv}{V_{LAA}} \tag{3.1}$$

$$v_{neck} = \frac{\int_{neck} |\vec{u}\vec{n}_{neck}|\, ds}{S_{neck}} \tag{3.2}$$

In Eq. 3.1, subscript LAA denotes that the integration is performed over the entire volume of the LAA and V_{LAA} represents the volume of the LAA. Similarly, in Eq. 3.2, subscript *neck* denotes that the integration is performed over the area of the cross-section plane at the neck region of the LAA and S_{neck} means the area of the plane. $\vec{n}_{neck}$ represents the unit normal vector on the plane pointing into the LAA. For the cases in the present study, the LAA neck cross-section planes are all defined manually so that they can naturally separate the LAA from the LA. Based on the definitions above, one can find that v_{ave} is the volume-averaged velocity magnitude over the whole LAA and v_{neck} is the area-averaged velocity magnitude along the $\vec{n}_{neck}$ direction over the LAA neck cross-section plane.

Time histories and time averaged data of v_{ave} and v_{neck} for each case are presented in Figure 3.3 and the values of some important hemodynamic parameters of four patient cases are listed in Table 3.1.

Table 3.1: Hemodynamic parameters for the four patient cases

	Patient-1	Patient-2	Patient-3	Patient-4
Stroke Volume (SV) (cm^3)	81.29	124.28	155.80	100.96
LA Volume (V_{LA}) (cm^3)	46.19	103.84	104.32	78.14
Relative Flow Rate (SV/V_{LA})	1.76	1.20	1.49	1.29
E/A Ratio	1.76	1.26	0.74	0.65

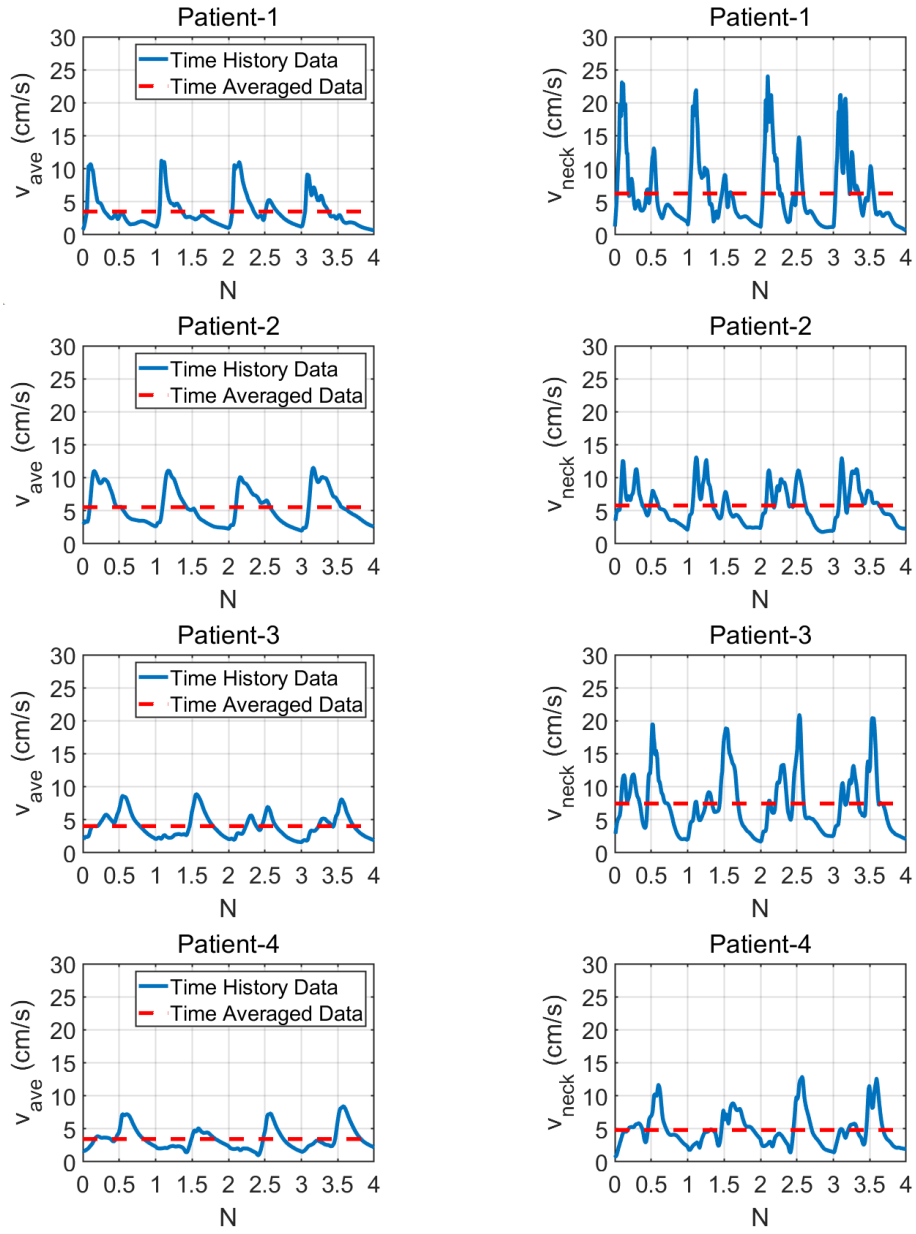

Figure 3.3: Time histories of v_{ave} and v_{neck} from the 4 patient-specific simulations, $N = \left(t - t_i^s\right) / T_i$, $i = 1, 2, 3, 4$

In Figure 3.3, N denotes for the cycle number and subscript s represents the start time instance. T denotes for the patient-specific cardiac cycle period and subscript i represents the i^{th} patient case. From the above plots, we can find that the time histories of v_{ave} and v_{neck} for the four cases have four similar peak regions, each of which corresponds to the simulation of one cardiac cycle. Inside one peak region, though not always clear for some cases, v_{ave} and v_{neck} usually have two peak values which correspond to the E-wave and A-wave respectively. However, due to the difference of the E/A ratios, the higher peak can be different from patient to patient. Since the E/A ratios of the Patient-1 and Patient-2 cases are larger than one, the values of v_{ave} and v_{neck} of the two cases tend to have a higher first peak during a cardiac cycle. On the contrary, for the Patient-3 and Patient-4 cases, as the E/A ratios of them are smaller than one, the peaks of v_{ave} and v_{neck} related to the A-wave are usually the higher ones.

Generally, for all cases, the peak values as well as the time averaged values of v_{neck} are always larger than those of v_{ave}, but the differences between the time averaged values of the two variables are small. Though the velocity boundary conditions at the MVO (see Figure 2.2) and the relative flow rate SV/V_{LA} (see Table 3.1) are different among all cases, the peak and averaged values of v_{ave} for each case are about the same order ($O(1)$), showing that the variable v_{ave} is not quite sensitive to either of them. Nevertheless, the peak values of v_{neck} are quite different among the above cases. From Figure 3.3, we can find a descending sequence of the four cases based on their peak values of v_{neck}. Not surprisingly, if we compare the four cases by their peak values

of the boundary velocity profiles from Figure 2.2 or by the relative flow rate SV/V_{LA} from Table 3.1, we can find the exactly same sequence of them. That means, unlike v_{ave}, the peak values of v_{neck} have a positive relation with the peak values of the velocity boundary conditions at the MVO and the relative flow rate SV/V_{LA}.

Based on the definitions and the quantitative analyses of v_{ave} and v_{neck} above, we believe that v_{ave} can be considered as an evaluation of the averaged flow intensity inside the LAA. While for v_{neck}, as it always has a higher value than v_{ave} and is an averaged velocity magnitude at the neck region of the LAA, it can be depicted as a variable that describes the relatively highest flow intensity in the LAA. Thus, both of them are related to the hemodynamics and the blood washout in the LAA, so they can be used to define the LAA hemodynamic metrics.

3.4 Scalar Concentration (C)

After we obtain the LAA hemodynamic metrics, we then need to look into the simulation results of the passive scalar transport so as to determine the blood washout rate metrics in the LAA. Initially, the passive scalar of each case is âĂIJfilledâĂİ into the LAA and the scalar concentration C in the LAA is set to be one (see Figure 2.3). To visualize the evolution of the passive scalar, the multi-layer iso-surface plots of C are presented in Figure 3.4 for all the patient cases at the end of each cardiac cycle.

Shown in Figure 3.4, as time goes, for all the cases, the passive scalar is continuously washed out from the LAA. However, due to the patient-specific

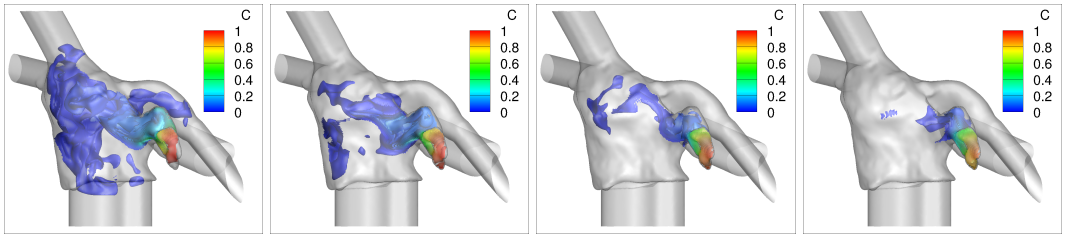

$N = 1,\ C_{va} = 0.48$ $N = 2,\ C_{va} = 0.33$ $N = 3,\ C_{va} = 0.25$ $N = 4,\ C_{va} = 0.22$

Patient-1

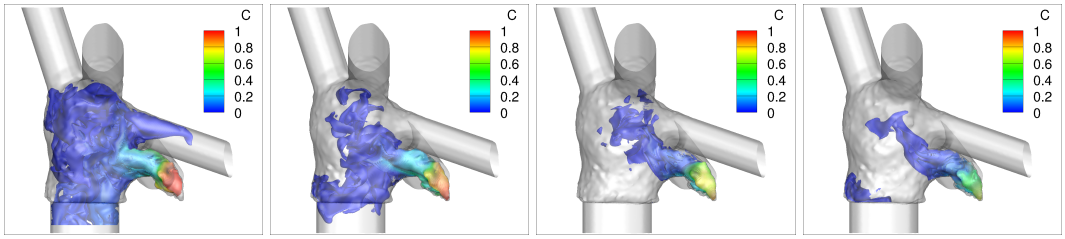

$N = 1,\ C_{va} = 0.48$ $N = 2,\ C_{va} = 0.31$ $N = 3,\ C_{va} = 0.20$ $N = 4,\ C_{va} = 0.13$

Patient-2

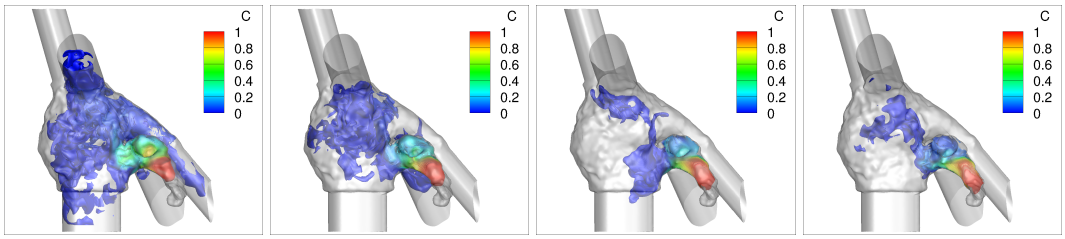

$N = 1,\ C_{va} = 0.63$ $N = 2,\ C_{va} = 0.49$ $N = 3,\ C_{va} = 0.41$ $N = 4,\ C_{va} = 0.35$

Patient-3

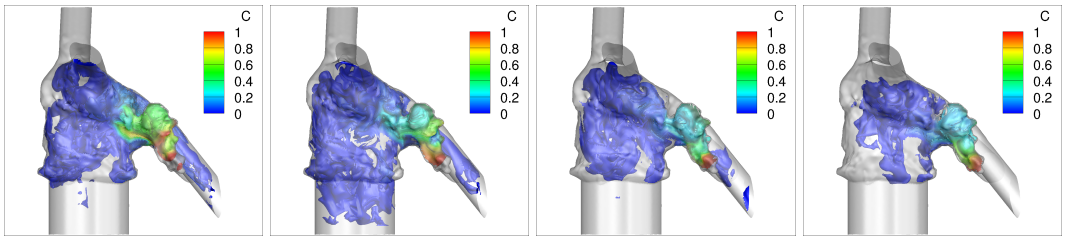

$N = 1,\ C_{va} = 0.63$ $N = 2,\ C_{va} = 0.48$ $N = 3,\ C_{va} = 0.41$ $N = 4,\ C_{va} = 0.34$

Patient-4

Figure 3.4: Washout of passive scalars

LAA geometry and the blood flow conditions, the final C_{va} in the LAA are different from patient to patient. By comparing the values of C_{va} at $N = 4$ among all the cases, Patient-3 has the largest final C_{va} while Patient-2 has the smallest final C_{va}. Moreover, the values of C also show that the passive scalar is not evenly distributed inside the LAA. As shown in Figure 3.4, the values of C at the tip of all the LAA are relatively higher than those at the neck region of the LAA. From the previous sections, one can find that the blood flow intensity is relatively low inside the LAA and the deeper you go into the LAA, the lower the flow intensity you will observe. This will affect the blood flow convection and inhibit the passive scalar transport, resulting in the non-uniform distribution of C inside the LAA.

To get the candidate variables for the blood washout rate metrics in the LAA, we need to quantify the washout rate of the passive scalar. Therefore, an exponential fitting method is then applied to the time histories of the passive scalar for all the cases in the next section.

3.5 Washout Rate in the LAA

To quantify the washout rate, the time history of the C_{va} in the LAA for each case is calculated and presented in Figure 3.5. An exponential decaying

function (Eq. 3.3) is then applied to fit with the data of each case.

$$
\begin{aligned}
&C_{va,i}(t) = A_i e^{-R_i\left(t-t_i^s\right)} + C_{va,i}^s - A_i \\
&A_i = \frac{C_{va,i}^e - C_{va,i}^s}{e^{-R_i\left(t_i^e - t_i^s\right)} - 1} \\
&C_{va,i}\left(t_i^s\right) = C_{va,i}^s,\ C_{va,i}\left(t_i^e\right) = C_{va,i}^e \\
&i = 1,\ 2,\ 3,\ 4
\end{aligned}
\tag{3.3}
$$

In Eq. 3.3, $C_{va,i}$ denotes for the C_{va} in the LAA for the i^{th} case and R represents the decay rate. A is a coefficient used to adjust the curve of each case to pass the first and the last data points. Superscripts s, e denote for the start and end time instances of each variable, respectively. The fitting results are presented in Figure 3.5 with red dashed curves.

For all cases, the exponential fittings have an average $\overline{r^2} \approx 0.95$, which demonstrates a good fitting quality. The inverse of the decay rate $1/R$ of each curve, which has the unit of time, can then be used as one of the metrics to evaluate the blood washout rate in the LAA. For example, if one patient case has an intense blood washout from LAA, the $1/R$ value will be expected to have a small value. On the contrary, if the blood washout is weak, the $1/R$ value should be high. In addition to $1/R$, the C_{va}^e of each case, which is the values of C_{va} at the end of the simulations, can also be considered as another metric for the blood washout rate in the LAA.

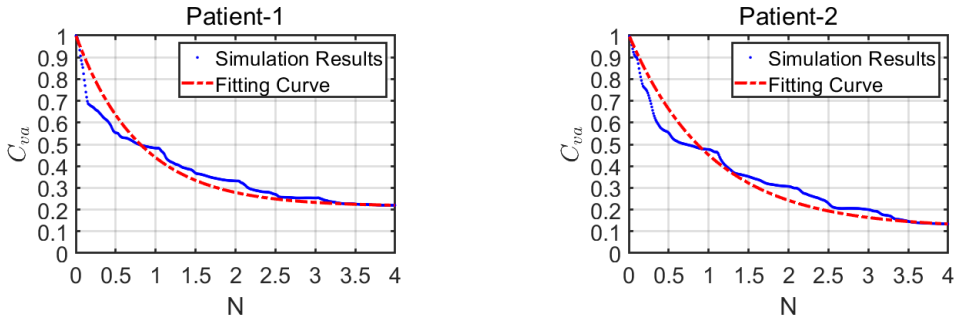

$\overline{r^2} = 0.91,\ R = 1.09, 1/R = 0.92$ $\overline{r^2} = 0.93,\ R = 0.89, 1/R = 1.12$

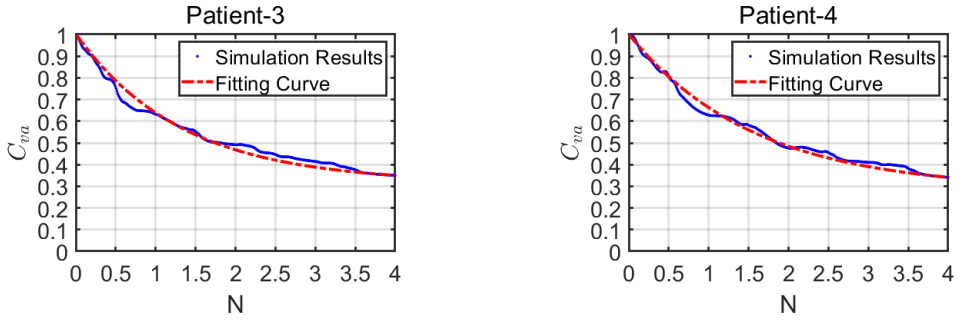

$\overline{r^2} = 0.98,\ R = 0.76, 1/R = 0.32$ $\overline{r^2} = 0.93,\ R = 0.75, 1/R = 1.34$

Figure 3.5: Exponential fittings for passive scalar washout

3.6 LAA Hemodynamic Metrics

With the simulation results above, two important averaged velocity variables, v_{ave} and v_{neck}, are defined and analyzed. Instead of directly using v_{ave} and v_{neck} as the LAA hemodynamic metrics, it is better to introduce some more parameters and derive the metrics with the same unit as the blood washout rate metrics. Since one of the blood washout rate metrics, $1/R$, has the unit of time, it is intuitive to define some length scale parameters from the morphology of the LAA and then combine with the velocity variables to derive some time-scale LAA hemodynamic metrics. Considering the geometry of the LAA, one possible way to define the length scale parameter is to use the volume (V_{LAA}), the neck cross section area (S_{neck}) and the surface area (S_{surf}) of the LAA. Specifically, two length scale parameters can be defined as

$$\begin{aligned} L_{surf} &= \frac{V_{LAA}}{S_{surf}}, \\ L_{neck} &= \frac{V_{LAA}}{S_{neck}}. \end{aligned} \tag{3.4}$$

In Eq. 3.4, L_{surf} represents the overall size of the LAA, while L_{neck} approximates the overall length of the LAA. Then, combined with v_{ave} and v_{neck}, two LAA hemodynamic metrics can be defined as

$$\begin{aligned} \tau_{ave} &= \frac{\int_{t^s}^{t^e} \frac{L_{surf}}{v_{ave}} dt}{t^e - t^s}, \\ \tau_{neck} &= \frac{\int_{t^s}^{t^e} \frac{L_{neck}}{v_{neck}} dt}{t^e - t^s}. \end{aligned} \tag{3.5}$$

Because v_{ave} and v_{neck} are functions of time, so in Eq. 3.5 we take the

time averaged of L_{surf}/v_{ave} and L_{neck}/v_{neck} from t^s to t^e. In the later section, correlations will be evaluated and shown between the blood washout rate metrics in the LAA ($1/R,\ C^e_{va}$) and the LAA hemodynamic metrics ($\tau_{ave},\ \tau_{neck}$) for all the cases. Before that, the scaled LAA cases are discussed first in the following section.

3.7 Additional Cases with Scaled LAA Models

Correlations with only the four cases above are, however, not very convincing. Thus, in order to add more data points as well as to study the effect of different LAA sizes on τ_{ave} or τ_{neck}, the LAA of Patient-1 and Patient-2 are approximately shrunk to 80% and enlarged to 120%, adding four more cases to the analysis. The 3D computer graphics software Blender is now used to complete the modification. The unstructured mesh of the LAA part is first selected and the volume of it is scaled to the desired percentages. The mesh of the neck region of the LAA will then be reconstructed and smoothed to guarantee the geometry continuity between the LA and the scaled LAA. The 3D anatomical models of the additional cases are presented in Figure 3.6.

Following this, similar simulations and analyses are performed with the four additional cases and the correlations now can be calculated with eight data points. Note that due to the highly non-linear nature of the fluid dynamics, it is not necessarily expected that this 20% changes will lead to a linearly proportional change in the metrics.

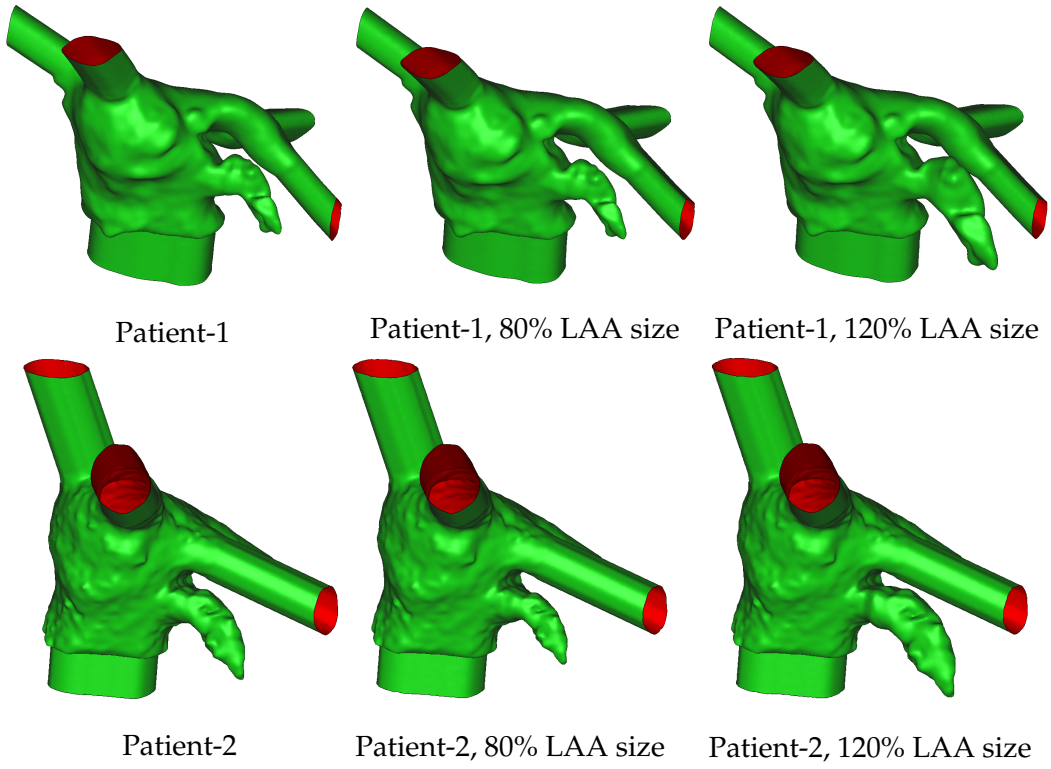

Figure 3.6: Anatomical models for scaled LAA cases

3.8 Correlations between Metrics

In this part, correlations between two groups of metrics will be established. The metrics are shown in Table 3.2 and the values of them for each case are shown in Table 3.3.

Table 3.2: Groups of metrics for correlations

Blood Washout Rate Metrics	LAA Hemodynamics Metrics
$\frac{1}{R}$, C_{va}^{e}	τ_{ave}, τ_{neck}

Table 3.3: Values of metrics for eight cases

	Patient-1	Patient-1, 80% LAA	Patient-1, 120% LAA
$(1/R)$ (s)	0.92	0.67	1.39
C_{va}^{e}	0.22	0.12	0.30
τ_{ave} (s)	0.047	0.029	0.053
τ_{neck} (s)	0.34	0.23	0.68

	Patient-2	Patient-2, 80% LAA	Patient-2, 120% LAA
$(1/R)$ (s)	1.12	0.50	1.12
C_{va}^{e}	0.13	0.029	0.14
τ_{ave} (s)	0.044	0.029	0.066
τ_{neck} (s)	0.34	0.22	0.48

	Patient-3	Patient-4
$(1/R)$ (s)	1.32	1.34
C_{va}^{e}	0.35	0.34
τ_{ave} (s)	0.066	0.059
τ_{neck} (s)	0.54	0.60

The resulting plots of the correlations between two metrics from the two groups respectively are then presented in Figure 3.7.

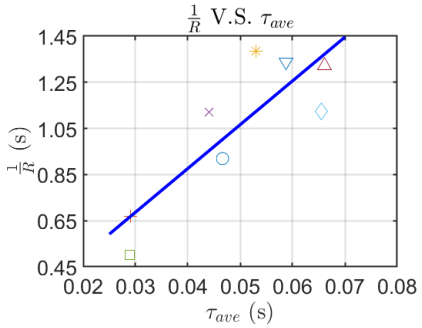

$r^2 = 0.73,\ p - value = 0.0069$

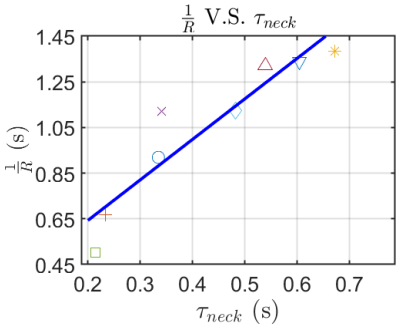

$r^2 = 0.87,\ p - value = 0.00076$

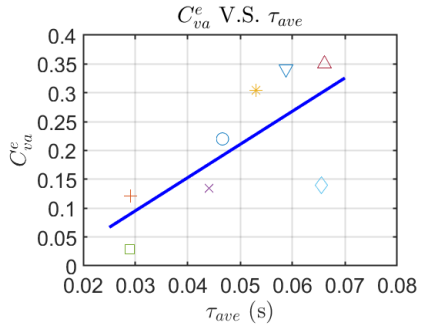

$r^2 = 0.51,\ p - value = 0.045$

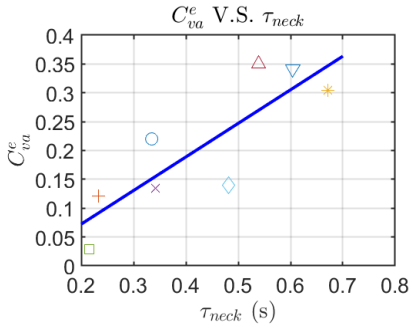

$r^2 = 0.72,\ p - value = 0.0081$

Averaged Fitting Quality: $\overline{r^2} \approx 0.71,\ \overline{p - value} \approx 0.015$

○ Patient-1; + Patient-1, 80% LAA; ✳ Patient-1, 120% LAA; × Patient-2; □ Patient-2, 80% LAA; ◊ Patient-2, 120% LAA; △ Patient-3; ▽ Patient-4; — Fitted Curves

Figure 3.7: Metrics correlations for eight cases

From the plots in Figure 3.7, the correlations between $1/R$ and τ_{neck} has the highest r^2 and the lowest $p-value$, indicating the best fitting quality and the highest correlation probability. Comparing the correlations with the blood washout rate metrics $1/R$ and C^e_{va}, one can find that those with $1/R$ have an averaged $\overline{r^2} \approx 0.80$ and an averaged $\overline{p-value} \approx 0.0038$, while those with C^e_{va} have an averaged $\overline{r^2} \approx 0.62$ and an averaged $\overline{p-value} \approx 0.027$, showing that the LAA hemodynamic metrics are better correlated with $1/R$ than with C^e_{va}. Moreover, for the LAA hemodynamic metrics τ_{ave} and τ_{neck}, the correlations with τ_{neck} have an averaged $\overline{r^2} \approx 0.80$ and an averaged $\overline{p-value} \approx 0.0044$, while those with τ_{ave} have an averaged $\overline{r^2} \approx 0.62$ and an averaged $\overline{p-value} \approx 0.026$, showing that the blood washout rate metrics are better correlated with τ_{neck} than with τ_{ave}. From the analysis above, one can see that τ_{neck} and $1/R$ may be a better metrics combination to predict the blood washout rate and the potential of thrombus formation in the LAA from patient-specific LAA hemodynamic conditions.

Naturally, with a larger LAA size, the blood washout rate in the LAA should decrease, since a larger volume of the LAA means a larger volume of blood needed to be washed out. As the washout rate decreases, the inverse of the scalar decay rate $1/R$ and the final values of the volume-averaged scalar concentration C^e_{va} should increase if they can correctly represent the washout rate in the LAA. The two LAA hemodynamic metrics τ_{ave} and τ_{neck} should also increase if they can correctly correlate with the washout rate metrics $1/R$ and C^e_{va}. Comparing the original and scaled LAA cases of Patient-1 and Patient-2 in Figure 3.7, we can find that under the same blood flow boundary

conditions, the larger the volume of LAA is, the larger the values of τ_{ave}, τ_{neck}, $1/R$ and C_{va}^{e} will be. This shows that the washout rate metrics in the LAA can correctly represent the washout rate and the LAA hemodynamic metrics can correctly correlate with the washout rate metrics. It also reveals that with a larger LAA size, the blood flow in the LAA tends to be more stagnant so the patient will have a higher potential of thrombus formation in the LAA.

Chapter 4

Limitation

In the present study, all the internal boundaries were considered stationary, which excluded the patient-specific LA motions. That is because the main focus of the present study is to find the blood washout rate metrics in the LAA and their correlations with the LAA hemodynamic metrics, and we believe that the LA/LAA motion will not alter the correlations we have found. Previous studies[5, 21] also have shown that including LA motions mainly influences the flow in the LA rather than in the LAA, and this should not influence the blood residence time and the washout rate in the LAA too much. However, we will investigate the effects of LA/LAA motion on blood washout rate and the correlations with the hemodynamic metrics in the future study.

It is also a limitation that the PV inlet boundary conditions are simplified by assuming zero-stress conditions in this study. A lumped element type model can be employed at these inlet boundaries to obtain more specific pressure boundary conditions. However, not only is it difficult to obtain patient-specific parameters for the lumped element model, this refinement will not have a huge impact on the flow patterns in the LA and the LAA. Therefore, the blood

washout rate in the LAA will also not be influenced significantly by such a change.

Though τ_{neck} shows an excellent correlation with the blood washout rate metric $1/R$, doing simulations and correlations with a total of eight cases is likely not enough to make it a general conclusion. Therefore, in the future, more patient-specific LA/LAA cases will be investigated, especially including the patient cases with the AF pathology.

Chapter 5

Conclusion

In this study, to investigate the blood washout rate in the LAA and to find the correlations with the LAA hemodynamic metrics, flow and passive scalar transport simulations are carried out for the patient-specific and scaled LA/LAA anatomical models also with the patient-specific velocity boundary conditions. According to the flow field observations, the blood flow inside the LAA is more stagnant than outside, showing a higher potential of thrombus formation. It also shows that the deeper you go into the LAA, the lower the flow intensity you will observe. Based on the quantitative analyses of the flow intensity, two averaged velocity variables are proposed to represent the averaged and the highest flow intensity in the LAA, respectively. Then, combined with the LAA geometry length parameters, the LAA hemodynamic metrics are defined for the correlations with the washout rate metrics.

As for the blood washout rate metrics in the LAA, by fitting an exponential function to the time history of the volume-averaged passive scalar concentration in the LAA for each case, the decay rates of the functions are obtained and the inverse of them are used for the metrics. Also, the final values of the

volume-averaged passive scalar concentration in the LAA can be considered as another metric.

Based on the two groups of metrics derived above, correlations between them are calculated and analyzed. The results show that the correlations with the inverse decay rate washout metric have better fitting quality than those with the final scalar concentration washout metric. The results also show that the correlations with the highest flow intensity metric are better than those with the averaged flow intensity metric. The most relevant correlation is the one between the inverse decay rate washout metric and the highest flow intensity metric.

Though in need of further improvement and more patient-specific cases to validate, the numerical approach developed in this study enables us to investigate the blood washout rate in the LAA and its relationship with the LAA hemodynamic metrics. It also provides insight into the development of new diagnostic method for the LAA thrombosis. According to the results and analyses above, it is shown that the LAA hemodynamic metirc related to the neck region of the LAA can be used as a good prediction of patient-specific blood washout rate, so it can also help predict the potential of thrombus formation in the patient-specific LAA. Thus, with a more reliable prediction, clinical decisions of individualized therapies to LAA diseases can be more effective.

Bibliography

[1] F. Triposkiadis, B. Pieske, J. Butler, J. Parissis, G. Giamouzis, J. Skoularigis, D. Brutsaert, and H. Boudoulas, "Global left atrial failure in heart failure," *European Journal of Heart Failure*, vol. 18, no. 11, pp. 1307–1320, 2016.

[2] D. Fatkin, R. P. Kelly, and M. P. Feneley, "Relations between left atrial appendage blood flow velocity, spontaneous echocardiographic contrast and thromboembolic risk in vivo," *Journal of the American College of Cardiology*, vol. 23, no. 4, pp. 961–969, 1994.

[3] L. Di Biase, P. Santangeli, M. Anselmino, P. Mohanty, I. Salvetti, S. Gili, R. Horton, J. E. Sanchez, R. Bai, S. Mohanty, A. Pump, M. Cereceda Brantes, G. J. Gallinghouse, J. D. Burkhardt, F. Cesarani, M. Scaglione, A. Natale, and F. Gaita, "Does the left atrial appendage morphology correlate with the risk of stroke in patients with atrial fibrillation? Results from a multicenter study," *Journal of the American College of Cardiology*, vol. 60, no. 6, pp. 531–538, 2012. [Online]. Available: http://dx.doi.org/10.1016/j.jacc.2012.04.032

[4] M. Prince, R. Bryce, E. Albanese, A. Wimo, W. Ribeiro, and C. P. Ferri, "The global prevalence of dementia: A systematic review and

metaanalysis," *Alzheimer's and Dementia*, vol. 9, no. 1, pp. 63–75.e2, 2013. [Online]. Available: http://dx.doi.org/10.1016/j.jalz.2012.11.007

[5] G. M. Bosi, A. Cook, R. Rai, L. J. Menezes, S. Schievano, R. Torii, and G. Burriesci, "Computational Fluid Dynamic Analysis of the Left Atrial Appendage to Predict Thrombosis Risk," *Frontiers in Cardiovascular Medicine*, vol. 5, no. April, pp. 1–8, 2018. [Online]. Available: http://journal.frontiersin.org/article/10.3389/fcvm.2018.00034/full

[6] G. García-Isla, A. L. Olivares, E. Silva, M. Nuñez-Garcia, C. Butakoff, D. Sanchez-Quintana, H. G. Morales, X. Freixa, J. Noailly, T. De Potter, and O. Camara, "Sensitivity analysis of geometrical parameters to study haemodynamics and thrombus formation in the left atrial appendage," *International Journal for Numerical Methods in Biomedical Engineering*, vol. 34, no. 8, p. e3100, 2018. [Online]. Available: https://onlinelibrary.wiley.com/doi/abs/10.1002/cnm.3100

[7] D. R. Holmes, D. R. Lakkireddy, R. P. Whitlock, R. Waksman, and M. J. Mack, "Left atrial appendage occlusion: Opportunities and challenges," *Journal of the American College of Cardiology*, vol. 63, no. 4, pp. 291–298, 2014.

[8] E. M. Hylek, C. Evans-Molina, C. Shea, L. E. Henault, and S. Regan, "Major hemorrhage and tolerability of warfarin in the first year of therapy among elderly patients with atrial fibrillation," *Circulation*, vol. 115, no. 21, pp. 2689–2696, 2007.

[9] J. M. Lee, J. Seo, J. S. Uhm, Y. J. Kim, H. J. Lee, J. Y. Kim, J. H. Sung, H. N. Pak, M. H. Lee, and B. Joung, "Why is left atrial appendage morphology related to strokes? an analysis of the flow velocity and orifice size of the left atrial appendage," *Journal of Cardiovascular Electrophysiology*, vol. 26, no. 9, pp. 922–927, 2015.

[10] R. Beigel, N. C. Wunderlich, S. Y. Ho, R. Arsanjani, and R. J. Siegel, "The left atrial appendage: Anatomy, function, and noninvasive evaluation," *JACC: Cardiovascular Imaging*, vol. 7, no. 12, pp. 1251–1265, 2014. [Online]. Available: http://dx.doi.org/10.1016/j.jcmg.2014.08.009

[11] P. Eslami, J.-H. Seo, A. A. Rahsepar, R. George, A. C. Lardo, and R. Mittal, "Computational Study of Computed Tomography Contrast Gradients in Models of Stenosed Coronary Arteries," *Journal of Biomechanical Engineering*, vol. 137, no. 9, p. 091002, 2015.

[12] J. H. Seo, T. Abd, R. T. George, and R. Mittal, "A coupled chemo-fluidic computational model for thrombogenesis in infarcted left ventricles," *American Journal of Physiology-Heart and Circulatory Physiology*, vol. 310, no. 11, pp. H1567–H1582, 2016. [Online]. Available: http://ajpheart.physiology.org/lookup/doi/10.1152/ajpheart.00855.2015

[13] T. M. van Bakel, K. D. Lau, J. Hirsch-Romano, S. Trimarchi, A. L. Dorfman, and C. A. Figueroa, "Patient-specific modeling of hemodynamics: Supporting surgical planning in a fontan circulation correction," *Journal of Cardiovascular Translational Research*, vol. 11, no. 2, pp. 145–155, 2018.

[14] L. T. Zhang and M. Gay, "Characterizing left atrial appendage functions in sinus rhythm and atrial fibrillation using computational models," *Journal of Biomechanics*, vol. 41, no. 11, pp. 2515–2523, 2008.

[15] R. Koizumi, K. Funamoto, T. Hayase, Y. Kanke, M. Shibata, Y. Shiraishi, and T. Yambe, "Numerical analysis of hemodynamic changes in the left atrium due to atrial fibrillation," *Journal of Biomechanics*, vol. 48, no. 3, pp. 472–478, 2015. [Online]. Available: http://dx.doi.org/10.1016/j.jbiomech.2014.12.025

[16] T. Otani, A. Al-Issa, A. Pourmorteza, E. R. McVeigh, S. Wada, and H. Ashikaga, "A Computational Framework for Personalized Blood Flow Analysis in the Human Left Atrium," *Annals of Biomedical Engineering*, vol. 44, no. 11, pp. 3284–3294, 2016.

[17] R. Mittal, H. Dong, M. Bozkurttas, F. M. Najjar, A. Vargas, and A. von Loebbecke, "A versatile sharp interface immersed boundary method for incompressible flows with complex boundaries," *Journal of Computational Physics*, vol. 227, no. 10, pp. 4825–4852, 2008.

[18] A. J. Chorin, "The numerical solution of the navier-stokes equations for an incompressible fluid," *Bulletin of the American Mathematical Society*, vol. 73, no. 6, pp. 928–931, 1967.

[19] C. Zhu, J. H. Seo, V. Vedula, and R. Mittal, "A Highly Scalable Sharp-Interface Immersed Boundary Method for Large-Scale Parallel Computers," no. June, pp. 1–10, 2017.

[20] A. F. Hall, J. A. Aronovitz, S. P. Nudelman, and S. J. Kovács, "Automated method for characterization of diastolic transmitral Doppler velocity contours: Late atrial filling," *Ultrasound in Medicine and Biology*, vol. 20, no. 9, pp. 859–869, 1994.

[21] C. Chnafa, S. Mendez, and F. Nicoud, "Image-based large-eddy simulation in a realistic left heart," *Computers and Fluids*, vol. 94, pp. 173–187, 2014. [Online]. Available: http://dx.doi.org/10.1016/j.compfluid.2014.01.030

CHUANXIN NI

322-O, Latrobe Hall, 3400 N. Charles Street, Johns Hopkins University ⋄ Baltimore, MD 21218
+1-443-467-0994 ⋄ cni7@jhu.edu

EDUCATION BACKGROUND

Whiting School of Engineering, Johns Hopkins University Aug. 2017 - Present
M.S. in Mechanical Engineering, Minor in Fluid Mechanics *Maryland, USA*

- **GPA**: 3.93/4.0
- **Advisor**: Rajat Mittal, Professor; Jung-Hee Seo, Associate Research Professor
- **Related Courses**: Fluid Dynamics I & II, Numerical Methods, Computational Fluid Dynamics, Finite Element Methods, Mathematical Methods of Engineering, Multiphase Flows

Honors College, Beihang University (211, 985 Project) Sept. 2013 - June, 2017
B.E. in Engineering Mechanics - Fluid Mechanics & Engineering *Beijing, China*

- **Overall GPA**: 89.43/100, 3.72/4.0; **Major GPA**: 91.74/100, 3.80/4.0; **Grade Rank:** 5/50
- **Related Courses**: Aerodynamics I & II, Computational Fluid Dynamics, Viscous Fluid Dynamics, Introduction to Turbulence, Numerical Methods

TOEFL IBT (Expired): **107** (R30 L27 S24 W26) GRE: **328** (V158 Q170 A/AW 3.5)

Grade for *Accent Reduction for ITAs*: **A**

PRESENTATION

1. **Ni, C.**, Seo, J. H., & Mittal, R. (2018). Computational modeling of hemodynamics and blood washout in the patient-specific left atrial appendages. *Bulletin of the American Physical Society.*

RESEARCH EXPERIENCE

Dept. Mechanical Engineering, Johns Hopkins University April, 2018 - Present
Student Researcher, Master's Thesis *Maryland, USA*

- **Project**: Computational modeling of hemodynamics and blood washout in the patient-specific left atrial appendages (LAA)
- *Advisor: Rajat Mittal, Professor;Jung-Hee Seo, Associate Research Professor;Johns Hopkins University*

- Constructed and modified 8 patients' left atrium geometry (LA) models by commercial software Materialise Mimics from patients' Computed Tomography (CT) scans;
- Extracted patient-specific velocity profiles from patients' Ultrasound Doppler Imaging data;
- Simulated blood flows including scalar transportation for patients by in-house immersed sharp interface DNS code (Vicar3D);
- Analyzed scalar washout rates from LAA by overall and piecewise fittings;
- Analyzed correlations between washout rates and patients' LAA medical information;
- Implemented inclined Neumann boundary conditions for in-house code (Vicar3D);

Dept. Mechanical Engineering, Johns Hopkins University Sept. 2017 - April, 2018
Student Researcher *Maryland, USA*

- **Project**: Blood flow simulations with intracranial aneurysms

· *Advisor: Rajat Mittal, Professor;Jung-Hee Seo, Associate Research Professor;Johns Hopkins University*

· Constructed patients' intracranial aneurysms geometry models from CT scans by Paraview;
· Built up internal sharp interfaces by using a Dynamic Growing Method and threshold control;
· Implemented Womersley pulsatile flow profile as a boundary conditions for in-house code (Vicar3D);
· Simulated blood flows with intracranial aneurysms and Womersley boundary conditions;
· Analyzed 3D velocity structure inside aneurysms.

Dept. Mechanical Engineering, Johns Hopkins University May, 2018
Student Researcher *Maryland, USA*

· **CFD Course Final Project**: 2D incompressible Navier-Stokes equations solver by immersed boundary method
· *Instructor: Jung-Hee Seo, Associate Research Professor;Johns Hopkins University*

· Discretized incompressible Navier-Stokes equations with a 1st order projection scheme (Non Van-Kan scheme);
· Solved the advection-diffusion equation by 2nd Adam-Bash and 2nd Crank-Nicolson schemes;
· Solved the pressure poisson equation by successive over-relaxation line Gauss-Seidel method;
· Represented the immersed boundary by volume penalization method;
· Tested the solver with 2D Cavity Flow and 2D Flow around A Circular Cylinder and compared results with references;

Dept. of Aeronautic Science and Technology Feb. 2017 - June, 2017
Student Researcher, Bachelor Dissertation *Beijing, China*

· **Project**: Research on Accuracy of Different Interpolation Algorithms Used in 1-D Overlapping Grids
· *Advisor: Zhengxun Gao, Associate Professor*

· Implemented 1D Euler equations solver by ENO/WENO algorithms in Fortran;
· Modified the solver to run on overlapping grids with different interpolation algorithms;
· Analyzed the accuracy of different interpolation algorithms with a 1D shock wave tube flow;

TEACHING

Dept. of Mechanical Engineering, Johns Hopkins University Sept. 2018 - Present
Teaching Assistant *Maryland, USA*

· Introduction to Fluid Mechanics; Instructor: Prof. Rajat Mittal

HONORS & AWARDS

Beihang University - Airbus Scholarship Oct. 2015

Beihang University Academic Excellence Scholarship Oct. 2015 & Oct. 2016

SKILLS

Commercial Software: Matlab, Ansys Workbench, Fluent, CFX, Tecplot, Solidworks, Blender, Mimics, 3-Matics
Programming Language: C, Fortran
Typesetting Language: LaTeX
Computational Simulation: Doing simulations on supercomputers with Linux OS